Mon. Not. R. Astron. Soc. **325,** 1065–1074 (2001)

Numerical simulations of weak lensing measurements

David J. Bacon,[1]★ Alexandre Refregier,[1] Douglas Clowe[2] and Richard S. Ellis[1,3]
[1]*Institute of Astronomy, Madingley Road, Cambridge CB3 OHA*
[2]*Max-Planck-Institut für Astrophysik, 85740 Garching, Germany*
[3]*California Institute of Technology, Pasadena CA 91125, USA*

Accepted 2001 March 14. Received 2001 March 14; in original form 2000 July 6

ABSTRACT

Weak gravitational lensing induces distortions on the images of background galaxies, and thus provides a direct measure of mass fluctuations in the Universe. The distortion signature from large-scale structure has recently been detected by several groups for the first time, opening promising prospects for the near future. Since the distortions induced by lensing on the images of background galaxies are only of the order of a few per cent, a reliable measurement demands very accurate galaxy shape estimation and a careful treatment of systematic effects. Here, we present a study of a shear measurement method using detailed simulations of artificial images. The images are produced using realizations of a galaxy ensemble drawn from the *Hubble Space Telescope* Groth strip. We consider realistic observational effects including atmospheric seeing, point spread function (PSF) anisotropy and pixelization, incorporated in such a manner as to reproduce actual observations with the William Herschel Telescope. By applying an artificial shear to the simulated images, we test the shear measurement method proposed by Kaiser, Squires & Broadhurst (KSB). Overall, we find the KSB method to be reliable with the following provisos. First, although the recovered shear is linearly related to the input shear, we find a coefficient of proportionality of about 0.8. In addition, we find a residual anti-correlation between the PSF ellipticity and the corrected ellipticities of faint galaxies. To guide future weak lensing surveys, we study the ways in which seeing size, exposure time and pixelization affect the sensitivity to shear. We find that worsened seeing linearly increases the noise in the shear estimate, while the sensitivity depends only weakly on exposure time. The noise is dramatically increased if the pixel scale is larger than that of the seeing. In addition, we study the impact both of overlapping isophotes between neighbouring galaxies, and of PSF correction residuals: together these are found to produce spurious lensing signals on small scales. We discuss the prospects of using the KSB method for future, more sensitive, surveys. Numerical simulations of this kind are a required component of present and future analyses of weak lensing surveys.

Key words: gravitational lensing – methods: data analysis – techniques: image processing – cosmology: observations – large-scale structure of Universe.

1 INTRODUCTION

Weak lensing provides a unique method with which to directly measure the mass fluctuations on large scales in the universe (see Mellier 1999; Kaiser 1999; Bartelmann & Schneider 2001 for recent reviews). This method relies on the measurement of small, coherent distortions produced by lensing upon the shapes of background galaxies. This effect is now routinely used to map the mass of clusters of galaxies (see reviews by Fort & Mellier 1994, Schneider 1996). Recently, the technique was extended to the field by several groups who reported the statistical detection of weak lensing by large-scale structure (Wittman et al. 2000; van Waerbeke et al. 2000; Bacon, Refregier & Ellis 2000, hereafter BRE; Kaiser, Wilson & Luppino 2000). More precise measurements of this 'cosmic shear' from upcoming observations will provide invaluable cosmological information (e.g. Kaiser 1992; Jain & Seljak 1997; Kamionkowski et al. 1998; Kaiser 1998; Hu & Tegmark 1999; van Waerbeke et al. 1999).

Because the distortions induced by lensing are only of the order of 1 per cent, these measurements are very challenging. In particular, they require tight control of systematic effects and a precise method for the measurement of the shear. One of the

★E-mail: djb@ast.cam.ac.uk (DJB)

potential weaknesses of the cosmic shear programme is the step leading from the measurement of the shapes of galaxies to the estimation of the lensing shear, in the presence of an anisotropic point spread function (PSF). The first method proposed with which to treat this problem was that by Bonnet & Mellier (1995). A more general, and now widely used, method was proposed by Kaiser, Squires & Broadhurst (1995, hereafter KSB) and further developed by Luppino & Kaiser (1997) and Hoekstra et al. (1998). Variations and alternatives to the KSB method have since been presented by Kaiser (2000), Rhodes, Refregier & Groth (2000) and Kuijken (1999).

In this paper, we address the ellipticity-to-shear problem using numerical simulations of artificial images. The numerical simulations which have been used for this purpose in the past have been derived either from *Hubble Space Telescope* (*HST*) images, degraded to match ground-based observations (e.g. KSB; Wittman et al. 2000), or by using *ab initio* artificial galaxy catalogues (e.g. Kaiser 2000). The former approach provides accurate shape statistics for the simulated galaxies, but can only produce a small simulated area. The latter approach allows the simulation of arbitrarily large areas, but is not necessarily as realistic. Because we are aiming at the demanding cosmic shear regime, we thus use a hybrid method in which large realizations of artificial galaxy images are drawn to reproduce the statistics of existing *HST* surveys.

Because it is widely used and more documented, we focus on the KSB method, and test its reliability in realistic observational conditions. For definitiveness, we consider the weak-lensing survey of BRE, who used ground-based observations with the William Herschel Telescope (WHT). We produce artificial galaxy catalogues generated from random realizations based on the *HST* Groth strip (Groth et al. 1994; Rhodes 1999). By applying artificial shears to the simulated images, we test both the systematic and statistical uncertainties of the method. We also investigate the way in which the shear signal degrades as a function of seeing, exposure time and pixel size. This is of considerable practical interest for the design of future weak lensing surveys. In addition, we examine the impact of overlapping isophotes on the shear signal, an effect which can potentially limit weak lensing measurements on small scales. An independent study of the shear measurement method using numerical simulations is presented in Erben et al. (2001).

The paper is organised as follows. In Section 2, we describe how we generate the artificial galaxy and star catalogues. In Section 3, we show how these are used to produced realistic images, which are compared to observed WHT images. This is followed in Section 4 by a brief description of our implementation of the KSB method. In Section 5, we present our results; the accuracy of recovery of shear with the KSB method is discussed, and the occurrence of an anti-correlation of shear with star ellipticity at low levels is noted. We demonstrate the degradation of the signal-to-noise ratio with increasing seeing, exposure time and pixel size, and also discuss the level at which overlapping isophotes will enhance the cosmological shear signal. The results are discussed and summarized in Section 6.

2 SIMULATED OBJECT CATALOGUE

The first step in these simulations is to construct an object catalogue. To do so, we used the image statistics from the Groth Strip, a deep survey taken with the *Hubble Space Telescope* (Groth et al. 1994; Rhodes et al. 2000). This *HST* survey is sampled at 0.1 arcsec and thus effectively gives us the unsmeared (i.e. before convolution with ground-level seeing) ellipticities and diameters of an ensemble of galaxies suitable for simulations of ground-based observations. The survey consists of a set of 28 contiguous pointings in *V* and *I*, with an area of approximately 108 arcmin^2 in a 3.5×44.0 arcmin region. The magnitude limit is $I \simeq 26$ (WFPC2 I band, F814W), and the strip includes about 10 000 galaxies.

We use a SExtractor (Bertin & Arnoults 1996) catalogue derived from the entire strip by Ebbels (1998). It contains, for each object, a magnitude determined by aperture photometry, and a diameter and ellipticity derived from second-order moments using a top-hat weight function. Armed with this catalogue, we model the multidimensional probability distribution of galaxy properties (ellipticity–magnitude–diameter) sampled by this catalogue. We find that the differential galaxy counts as a function of *I* magnitude are well described by

$$\frac{\mathrm{d}n}{\mathrm{d}I} \simeq 10^{(a_0 + a_1 I + a_2 I^2)} \,\mathrm{galaxies\,deg^{-2}\,mag^{-1}},$$

with $a_0 = -19.0$, $a_1 = 1.64$ and $a_2 = -0.027$; the radius distribution is modelled as $r = 0.095 \times 10^{(b_1 + b_2 I + b_3)}$ arcsec with $b_2 = -0.14$ and with b_1 a Gaussian distribution with mean 3.75 and rms 0.098. Ellipticity components e_1 and e_2 are described by Gaussian probability distributions of rms 0.34, and the position angle is randomly chosen. We draw from this modelled distribution a catalogue of galaxies statistically identical to the Groth strip distribution by Monte Carlo selection.

For definiteness, we aim to reproduce the conditions of our weak lensing survey derived from observations with WHT (see BRE). This survey consisted of 14 independent blank fields observed with the WHT prime focus CCD Camera (field of view 8×16 arcmin^2, pixel size 0.237 arcsec, EEV CCD) in the *R* band. A relevant issue is the number of stars obtained: by tuning the Galactic latitude ($30° < b < 70°$), we required the fields to contain $\simeq 200$ stars with $R < 22$ in order to map carefully the PSF and the camera distortion across the field of view. The integration time on these fields was 1 h, affording a magnitude limit of $R = 25.2$ (all *R* magnitudes quoted as Vega magnitudes).

Given that the Groth strip is in *I* while our data are in *R*, we allowed a slight increase (multiplication by 1.2) to radius with magnitude to better model the WHT images; this factor has been included in the described model above. The number density–magnitude dependence was found to fit very well without alteration.

We spatially distribute the galaxies with a uniform probability across the field of view. Since the Groth strip does not contain enough stars to create a good model, star counts with *R*-magnitude are modelled as a power law [$(\mathrm{d}n)/(\mathrm{d}R) \propto R^{0.2}$] which is found to be a good fit to the WHT data.

We assign a morphological class (elliptical, spiral or irregular) for future image realization to each galaxy using the results of Abraham et al. 1996). Specifically, we use their measured fraction for each class as a function of magnitude. After application of all of the above procedures, we obtain our unlensed object catalogues.

To produce the lensed object catalogue, we sheared the galaxies in the catalogue by calculating the change in the object ellipticity arising from lensing. This was done using the relation (Rhodes et al. 2000)

$$e_i' = e_i + 2(\delta_{ij} - e_i e_j)\gamma_j. \quad (1)$$

Since we are primarily interested only in the mean shear measured

on the field, we chose the imposed shear to be uniform over a given field.

Note that we do not include an extra shear arising from telescope optics, over and above the shear already imposed to mimic the cosmological signal. BRE (2000) shows how we deal with this systematic effect; since we can very precisely quantify the telescope shear, and since we simply subtract it from the overall shear measured, we do not discuss it further in this paper.

Stellar ellipticities (simulating tracking errors, atmospheric effects, etc.) are similarly chosen as uniform over a given field (see below for how the PSF is realized). The ellipticity for each field is taken from a Gaussian probability distribution with a standard deviation of $\sigma_e^* = 0.08$. This is conservatively chosen to be slightly worse than the rms stellar ellipticity of the stars in our WHT survey, for which $\sigma_e^* \simeq 0.07$.

3 IMAGE REALIZATION

We create the artificial images using the IRAF ARTDATA package. This takes the star and galaxy catalogues and plots the objects with specified positions, ellipticity, magnitude, diameter and morphology. Only exponential discs and de Vaucouleurs profiles are supported. We model ellipticals and irregulars as de Vaucouleurs profiles, and spirals as exponential discs.

Each pixel in these simulations is subdivided into a 10×10 grid of subpixels. The appropriate subpixel flux for a star or galaxy is calculated from the analytical intensity profile, and the PSF convolution is similarly performed at the subpixel level.

We use the package to recreate several WHT-specific details: the magnitude zero point is chosen to match the telescope throughput, the stars and galaxies are convolved with the chosen elliptical PSF (seeing chosen to be 0.8 arcsec unless otherwise specified, ellipticity dispersion 0.08), the image is appropriately pixellized (0.237 arcsec per pixel), Poisson photon noise for objects and sky background are included, and Gaussian CCD read noise (3.9 electrons) are added. The appropriate gain [1.45 electrons/analogue-digital unit (ADU)] is included, and an appropriate sky background (10.7 ADU s^{-1}) is imposed. The PSF profile chosen is the Moffat profile, $I(r) = [1 + (2^{1/\beta} - 1)(r/r_{\rm scale})^2]^{-\beta}$, where $\beta = 2.5$ and $r_{\rm scale}$ is the seeing radius. The generalized radius r is the distance from the centroid, transformed so that the profile is elliptical. This profile has wings which fall off more slowly than for a Gaussian profile, and provides a good description of our seeing-dominated PSF, which has an elliptical, concentric profile with extended wings.

An observed WHT image is shown in Fig. 1, which may be compared with an example 4×4 arcmin^2 portion of a 16×8 arcmin^2 simulated field is shown in Fig. 2. A global impression can be obtained from the full 16×8 arcmin^2 fields plotted in BRE. The simulated image lacks saturated stars ($R \lesssim 18$); these are, by construction, absent from the simulated catalogue (see size–magnitude figure in BRE), since such stars cannot be used in our weak lensing analysis, and would be immediately excised if present. The galaxy images appear to be very similar in the simulations as compared with the data.

To compare these images quantitatively, we derived a measured object catalogue using the IMCAT routines (see Section 4 below for details). They provide the position, magnitude, half-light radius, ellipticity and polarizability tensors for each object detected on the image.

The resulting distribution on the radius–magnitude plane is shown in section 7 of BRE for both a simulated field and the

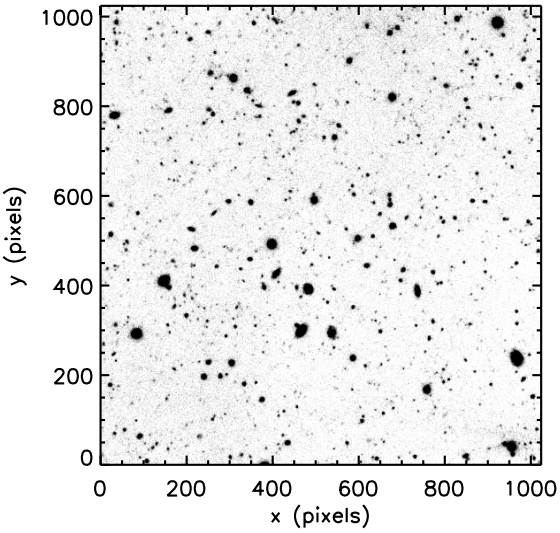

Figure 1. Detail of a real data image (WHT3). The area displayed is 4×4 arcmin^2, while the full image is 8×16 arcmin^2.

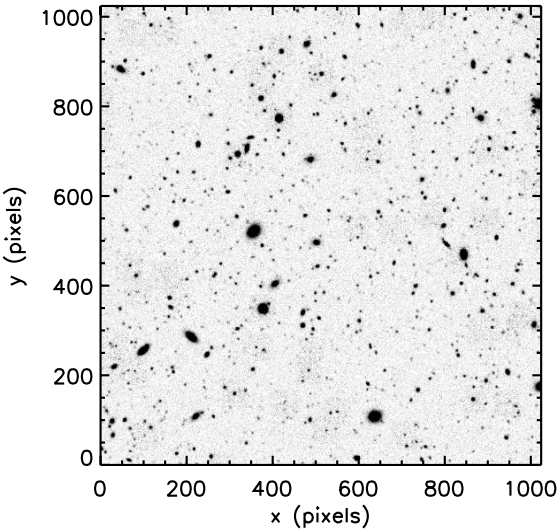

Figure 2. Detail (4×4 arcmin^2) of a simulated image.

observed WHT field; the running mean and standard deviation of $r_{\rm g}$ with magnitude is shown on Fig. 3. The distributions are similar, with the mean radius agreeing to within 0.2 pixel throughout the magnitude range. The rms scatter in radius is somewhat larger at faint magnitudes for the real data, as a result of the response of the measurement software to the simple smooth profiles used in the simulations.

Fig. 4 compares differential number counts with R magnitude for the simulations and real data. The counts derived from the simulated image and from our real R-band fields agree very well; the simulated image counts also agree well with the simulated catalogue counts, with an unsurprising turn-over near the expected magnitude completeness limit for the 1-h exposure time ($R \lesssim 25$). The simulations' close impersonation of real data number counts is of importance for obtaining realistic results for, e.g., overlapping isophotes in section 5.

Fig. 5(a) shows the ellipticity (e_1) distributions $f(e_1)$ for the *initial* simulated catalogue, and the *smeared* simulated and real objects. The distributions were normalized so that $\int {\rm d}e_1 \; f(e_1) \equiv 1$.

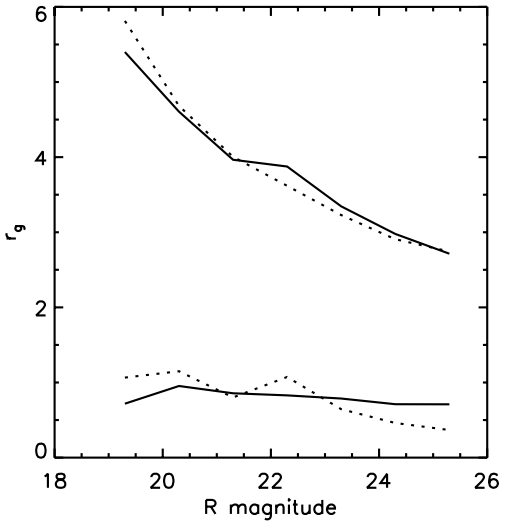

Figure 3. Galaxy size statistics with *R* magnitude. The upper curves show the mean filter radius r_g in unit magnitude bins; solid line shows real data, dotted line shows simulated data. The lower curves show the standard deviation on the radius in unit magnitude bins.

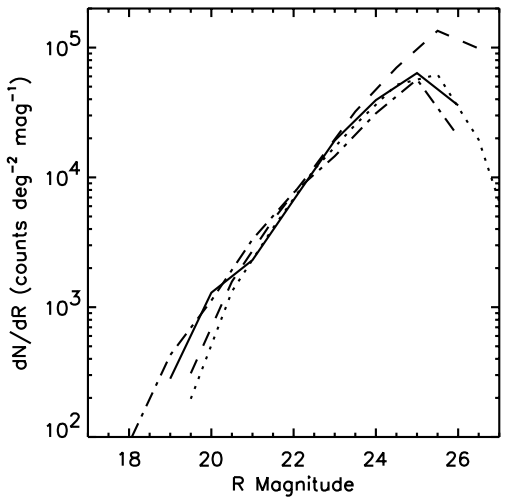

Figure 4. Differential galaxy number counts with *R*-magnitude (except for real Groth data in *I*). Real WHT data (WHT3) is shown as solid line; Groth strip number counts are shown as dash-dotted. The counts for the simulated catalogue are shown dashed, and those recovered by KSB from the simulated images is shown dotted.

As expected, smearing reduces the ellipticity dispersion. The simulated and real smeared distributions are remarkably similar. See section 5 for further discussion on this point.

4 SHEAR MEASUREMENT METHOD

Our shear measurement method is a version of the KSB method and was described in detail in BRE. Here we summarize it and then describe the relevant details of our specific implementation.

4.1 Overview of the KSB method

The KSB method derives the shear from the ellipticity of galaxies, after correcting for the smearing by the PSF. We use the implementation of the KSB method achieved by the IMCAT software kindly provided to us by Nick Kaiser.

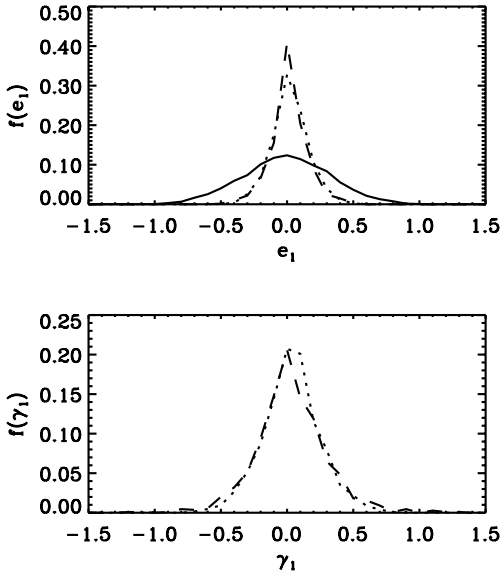

Figure 5. Comparison of shape measures. The top panel shows the normalized ellipticity e_1 distribution for initial unsmeared simulated catalogue (solid) and smeared simulated (dotted) and real (dashed) objects. The bottom panel shows the distribution of the shear estimators for corrected simulated (dotted) and real (dashed) objects.

The routine HFINDPEAKS first finds objects in each field by convolving the image with smoothing kernels of different sizes. The object radius r_g is defined by the size of the kernel which maximizes the signal-to-noise ratio, ν, of the object. The routine GETSHAPES then takes r_g as the size of the Gaussian weight function used to measure quadrupole moments I_{ij} of the object about its centre of light. The ellipticity of the object is then defined as $e_i \equiv \{I_{11} - I_{22}, 2I_{12}\}/(I_{11} + I_{22})$.

The next step in the KSB algorithm is to correct for the anisotropy of the PSF. The corrected ellipticity of a galaxy $e^{\rm g}_{\rm corrected}$ is related to the observed smeared ellipticity $e^{\rm g}_{\rm smeared}$ by

$$e^{\rm g}_{\rm corrected} = e^{\rm g}_{\rm smeared} - P^{\rm g}_{\rm sm} p, \tag{2}$$

where the ellipticities are understood to denote the relevant two-component spinor e_i, and p is a measure of PSF anisotropy. The tensor $P^{\rm g}_{\rm sm}$ is the smear polarizability, a 2×2 matrix with components involving higher moments of surface brightness. Since for stars $e^{*}_{\rm corrected} = 0$, p can be measured using

$$p = (P^{*}_{\rm sm})^{-1} e^{*}_{\rm smeared}. \tag{3}$$

The lensing shear takes effect before the circular smearing of the PSF. Luppino & Kaiser (1997) showed that the *pre*-smear shear γ averaged over a field can be recovered using

$$\gamma = P^{-1}_{\gamma} e^{\rm g}_{\rm corrected}, \tag{4}$$

where

$$P_{\gamma} = P^{\rm g}_{\rm sh} - \frac{P^{*}_{\rm sh}}{P^{*}_{\rm sm}} P^{\rm g}_{\rm sm}. \tag{5}$$

Here, $P^{\rm g}_{\rm sh}$ is the shear polarizability tensor for the galaxy involving other higher-order moments of the galaxy image. The quantities $P^{*}_{\rm sh}$ and $P^{*}_{\rm sm}$ are the shear and smear polarizabilities calculated for a star interpolated to the position of the galaxy in question. With the smear and shear polarizabilities calculated by IMCAT, we can therefore find an estimator for the mean shear in a given cell.

4.2 Specific implementation

First, we need to remove noisy detections. We applied a size limit $r_g > 1.0$ to initially reject extraneous detections of very small objects claimed by IMCAT. We also applied a signal-to-noise ratio $\nu > 15.0$ limit (see Section 5.2 for justification of this apparently very conservative cut). To reduce the noise in our measurement, we also remove highly elliptical objects with $e > 0.5$.

Stars were identified using the non-saturated stellar locus on the magnitude–r_h plane (see fig. 11 in BRE), typically with $R \simeq 19$–22. In the data, the stellar ellipticity is a smooth function of position on the field. We thus adopted an iterative interpolation scheme to model this variation. Specifically, we first fitted a two-dimensional cubic function to the measured stellar ellipticities, plotted the residual ellipticities $e^{\rm res} = e^* - e^{\rm fit}$ and re-fitted after the removal of extreme outliers (caused by galaxy contamination, blended images and noise). The stellar ellipticity was kept constant in the simulations, but we nevertheless fit the two-dimensional (2D) cubic for correction, as a means of retaining potential systematic effects induced in this step.

In order to correct galaxies for anisotropic smear, we need not only the fitted stellar ellipticity field, but also the four component stellar smear and shear polarizabilities as a function of position. Here a 2D cubic is fit for each component of $P^*_{\rm sm}$ and $P^*_{\rm sh}$. Galaxies are then chosen from the magnitude–r_h diagram by removing the stellar locus and objects with $\nu < 15$, $r_g < 1$, $e > 0.5$, as described above. From our fitted stellar models, we then calculate e^*, $P^*_{\rm sm}$ and $P^*_{\rm sh}$ at each galaxy position, and correct the galaxies for the anisotropic PSF using equation (2). As a result, we obtain $e^{\rm g}_{\rm corrected}$ for all selected galaxies in each cell.

We then calculate P_γ for the galaxies. We opt to treat $P^*_{\rm sh}$ and $P^*_{\rm sm}$ as scalars equal to half the trace of the respective matrices. This is allowable, since the non-diagonal elements are small and the diagonal elements are equal within the measurement noise (typical $P^*_{sm,11,22} = 0.10$, $P^*_{sm,12,21} < 5 \times 10^{-4}$, $P^*_{sh,00,11} = 1.1$, $P^*_{sh,12,21} < 0.01$).

With this simplification, we calculate P_γ according to equation (5). P_γ is typically a noisy quantity, so we fit it as a function of r_g. P_γ also has a scatter in magnitude and significance ν, but we find that a simple fit with r_g alone reduces the scatter of P_γ versus magnitude by a factor of 2; more importantly, we find that this fit affords shear recovery with manageable noise, while keeping to the simplest possible procedure.

We choose to treat P_γ as a scalar, since the information it carries is primarily a correction for the size of a given galaxy, regardless of its ellipticity or orientation. We thus plot P^{11}_γ and P^{22}_γ together against r_g, and fit a cubic to the combined points. Moreover, since P_γ is unreliable for objects with r_g measured to be less than r^*_g, we remove all such objects from our prospective galaxy catalogue.

Finally, we calculate a shear measurement for each galaxy as in equation (4), where the P_γ is the fitted value for the galaxy in question.

Because of pixel noise, a few galaxies yield extreme, unphysical, shears γ. To prevent these from unnecessarily dominating the analysis, we have removed galaxies with $\gamma > 2$.

This entire procedure provides us with an estimator of the shear γ for each galaxy. We can also calculate the mean shear $\bar\gamma = \langle\gamma\rangle$ in a cell and its associated error $\sigma[\bar\gamma] = \sigma[\gamma]/\sqrt{N}$, where N is the number of galaxies in a cell.

5 RESULTS

5.1 Ellipticity distribution

We first compare the distribution of ellipticities and shear estimators within a field. As we noted above, the uncorrected ellipticity distribution of the simulated objects is very similar to that of the data (Fig. 5a). The distribution of the shear estimators γ_1 after all corrections is shown in Fig. 5(b), for each case. The agreement is good, showing that the simulations faithfully reproduce the shape statistics of the data, the central concern for weak lensing.

Table 1. Ellipticity and shear rms dispersion at different stages of the correction method.

dispersion	simulation	data
σ_e (input)	0.47	
σ_e (measured)	0.20	0.20
σ_γ (final)	0.31	0.39

In general, the variance of the shear estimators results from several effects: the intrinsic ellipticity dispersion, pixelization, and pixel noise. The latter effect is enhanced by the correction for the isotropic smearing. The ellipiticity and shear rms dispersion, $\sigma_e \equiv \langle e^2\rangle^{1/2}$ and $\sigma_\gamma \equiv \langle\gamma^2\rangle^{1/2}$, at different stages of the correction algorithm are listed in Table 1. The ellipticity dispersion observed in the simulated image is reduced by the PSF smearing as compared to the input ellipticity dispersion. (Pixel noise and pixelization tends to increase the observed dispersion, but the smearing dominates.) The smearing is corrected for by the KSB method, leading to a re-increased dispersion σ_γ in the corrected shear estimator.

We can obtain an estimate of the relative contribution of pixel noise and intrinsic dispersion using these results. In the absence of weighting and smearing, the ellipticity is related to the shear by $\epsilon = g\gamma$, where $g = (2 - \langle\epsilon^2\rangle)$ (see equation 1 and Rhodes et al. 2000). For the simulations, the input ellipticity dispersion is $\sigma_e \simeq 0.47$, yielding $g \simeq 1.8$. As a result, the shear rms produced by the intrinsic dispersion alone is $\sigma^{\rm intrinsic}_\gamma \approx \sigma^{\rm input}_e/g \simeq 0.26$. The fact that this value is close to the total shear disperion $\sigma_\gamma \simeq 0.31$ observed in the simulations shows that the intrinsic dispersion is larger than, but comparable to, that produced by pixel noise and pixelization. These considerations should be kept in mind in planning the exposure time of weak lensing surveys. We will study the impact of worsened seeing and larger pixel sizes in Sections 5.4 and 5.6.

5.2 Test of the anisotropic correction

Before we discuss the reclamation of shear, we address the existence of a remaining systematic effect. In BRE, we found that a signal-to-noise ratio cut of $\nu > 5$ (as opposed to our conservative $\nu > 15$) reveals a strong anti-correlation between the mean shear $\bar\gamma_i$ and the mean stellar ellipticity $\bar e^*_i$. Here we show that the same effect is found in the simulated data. Fig. 6 shows $\bar\gamma_i$ versus $\bar e^*_i$ for 20 simulated fields, which exhibit similar behaviour to that found in BRE section 6 for real fields. To assess the significance of this effect, we use the correlation coefficient

$$C_i = \frac{\langle e^*_i\,\gamma_i\rangle - \langle e^*_i\rangle\langle\gamma_i\rangle}{\sigma(e^*_i)\sigma(\gamma_i)}. \quad (6)$$

For a $\nu > 5$ cut we find $C_1 = -0.69$, $C_2 = -0.81$ for 20 cells, which corresponds to a $\gg 3\sigma$ effect as for the real data. A cut at $\nu > 15$ reduces the anti-correlation to $C_1 = -0.32$, $C_2 = -0.48$.

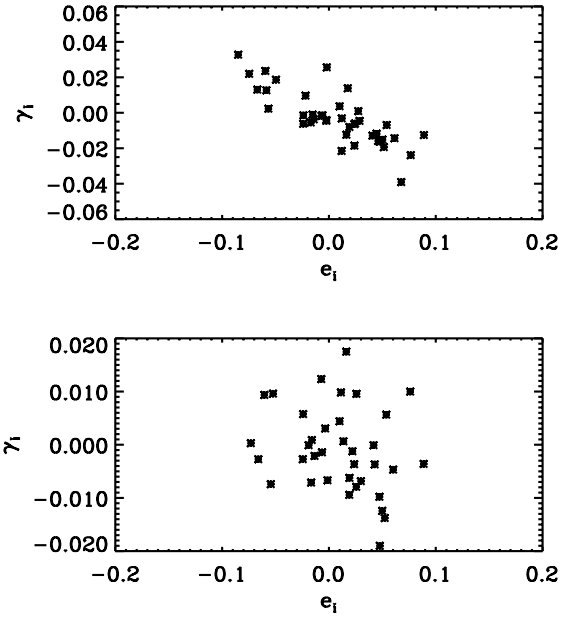

Figure 6. The anti-correlation of $\bar{e}_i^*$ and $\bar{\gamma}_i$ plotted for 20 simulated fields, where i $= 1, 2$ have been superposed, for (top) a $\nu > 5$ cut, and (bottom) a $\nu > 15$ cut. Note the trend for $\nu > 5$.

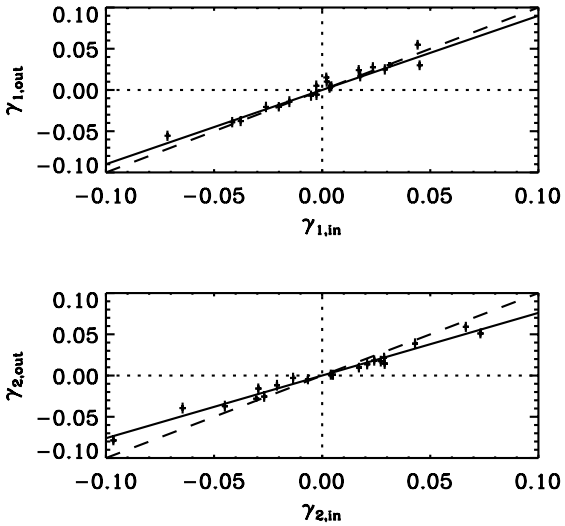

Figure 7. $\gamma_i^{\rm in}$ compared with $\gamma_i^{\rm out}$ for simulated data sheared by 5 per cent rms shear; top panel shows γ_1 input and output, while bottom panel shows γ_2 component. Each point corresponds to one of the simulated fields. The dashed line shows the $\gamma_i^{\rm in} = \gamma_i^{\rm out}$ relation; the solid lines shows the best fits, $\gamma_1^{\rm in} = 0.90\gamma_1^{\rm out}$ and $\gamma_2^{\rm in} = 0.76\gamma_2^{\rm out}$.

This corresponds to a 1.5–2σ effect, which is no longer a significant contribution to the lensing amplitude. This anti-correlation is thus the result of an over-correction of the PSF for small galaxies (in equation 2). This is likely to arise from the fact that, because of noise, the observed radius [and thus $(P_{\rm sm}^{\rm g})^{-1}$] of faint galaxies is slightly smaller than that of the bright stars used to measure the PSF. Note that Fig. 6 is very similar to the equivalent figure in BRE section 6 for real data. This again confirms the validity of the simulations and their use in testing systematic effects, and verifies that the low-level anti-correlation found in real data stems from a reproducible problem with the current correction method.

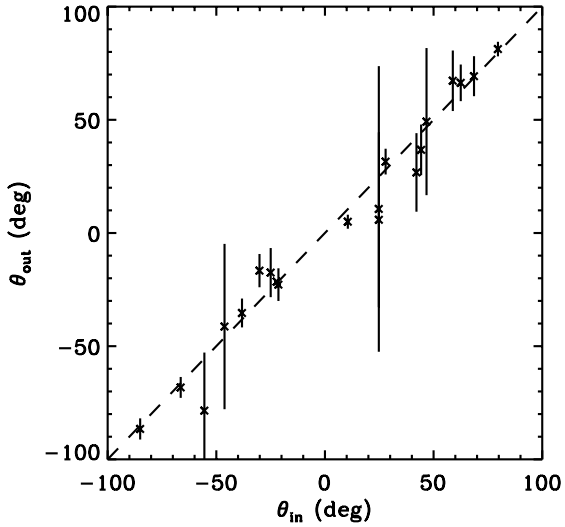

Figure 8. Input shear orientation compared with output shear orientation for simulated data sheared by 5 per cent rms shear. The dashed line shows the $\theta_{\rm in} = \theta_{\rm out}$ relation, which is the best fit.

5.3 Shear recovery

We now wish to observe how the output shear derived by the KSB algorithm compares to the shear input. In order to test this, we ran a set of simulations with 5 per cent rms shear for 20 fields, following the simulation and recovery procedures of Sections 2 to 4. More precisely, for each field we drew a uniform shear from a Gaussian probability distribution, with standard deviation equal to a shear of 0.05. A similar set of 30 fields were simulated with 1.5 per cent rms shear. For all of these simulations, we include the systematic effects described in Section 3, such as anisotropic PSF (seeing 0.8 arcsec), and run the full recovery and correction algorithm described in Section 4.

Our results for the 5 per cent simulations are shown in Fig. 7 (see also section 7 in BRE for a summary). The figure shows that the output shear is clearly linearly related to the input shear, with a slope close to 1. As a quantitative test, we apply a linear regression fit to both components of the shear, combined and separately. For the combined components we obtain $\gamma_i^{\rm out} = 0.0007 + 0.84\gamma_i^{\rm in}$, with standard errors on the coefficients of 0.001 and 0.04, respectively. For the individual components we obtain $\gamma_1^{\rm out} = 0.002 + 0.90\gamma_1^{\rm in}$ with errors (.001, .05) and $\gamma_2^{\rm out} = 0.0001 + 0.76\gamma_2^{\rm in}$ with errors (.001, .04). For the 1.5 per cent simulations we similarly obtain consistent results, namely $\gamma_i^{\rm out} = 0.0001 + 0.79\gamma_i^{\rm in}$ for combined components with respective standard errors of 0.001 and 0.091.

Fig. 8 shows the input versus output orientation of the shear (angle anticlockwise from x-axis). Note that this is virtually unbiased without correction [$\theta_{\rm out} = (1.00 \pm 0.05)\theta_{\rm in}$] and equally so with division by the factors described [$\theta_{\rm out} = (0.99 \pm 0.04)\theta_{\rm in}$]. Thus we see that there is only a calibration issue in shear amplitude, not shear orientation, in this implementation of KSB.

We see that the IMCAT measure of shear is symmetrical about zero, but is measuring a slightly smaller shear signal than the input shear. In similar conditions, we should therefore adjust our shear measures by dividing γ_1 by 0.9 ± 0.05 and γ_2 by 0.76 ± 0.04 when using this KSB implementation. However, one should recognize that these factors are only suitable in the selected conditions; further simulations are necessary for other regimes of seeing, pixelization and shear.

Table 2. Shear sensitivity as a function of seeing, in 8×8-arcmin^2 cells.

Seeing ($''$)	n_g (arcmin^{-2})	σ_γ	σ_{noise}	Median R	Median z	σ_{lens}	S/N
0.4	29.8	0.43	0.0097	24.1	0.8	0.0096	1.0
0.8	18.0	0.44	0.0130	23.4	0.8	0.0096	0.7
1.2	11.8	0.46	0.0168	22.8	0.7	0.0086	0.5
1.6	7.5	0.49	0.0225	22.2	0.6	0.0076	0.3
2.0	5.2	0.50	0.0275	21.9	0.6	0.0076	0.3

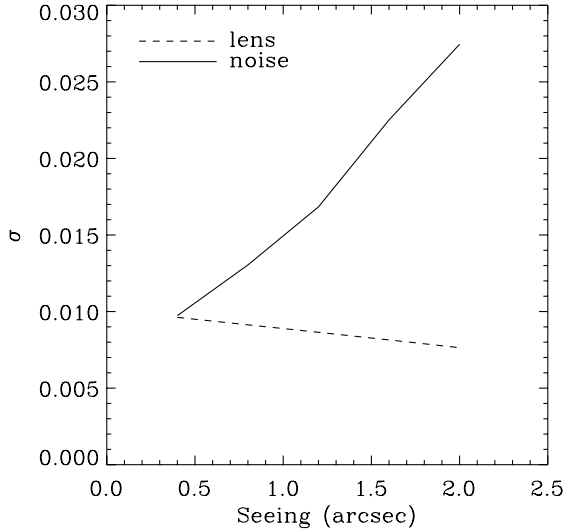

Figure 9. σ_{noise} (solid) and σ_{lens} (dashed) as a function of seeing FWHM for a set of simulations with 1-h integration times. Note the steady degradation of sensitivity with seeing.

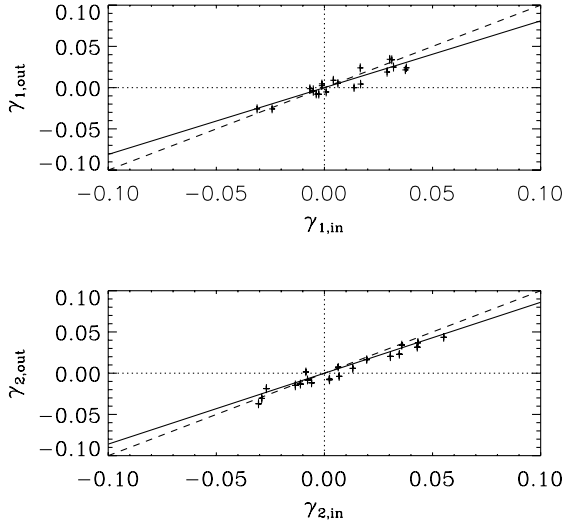

Figure 10. γ_i^{in} compared with γ_i^{out} for simulated data sheared by 5 per cent rms shear in 0.4-arcsec seeing; as before, top panel shows γ_1 input and output, while bottom panel shows γ_2 component. The dashed line shows the $\gamma_i^{in} = \gamma_i^{out}$ relation; the solid lines show the best fits, $\gamma_1^{in} = 0.81\gamma_1^{out}$ and $\gamma_2^{in} = 0.86\gamma_2^{out}$.

A full discussion of the recovery of rms shears using an extensive statistical analysis can be found in BRE, including a discussion of the recovery of rms shears from sets of simulated fields.

5.4 Effect of seeing

Of great practical interest is the dependence of the sensitivity of weak lensing measurements on seeing. To study this dependence, we ran several simulations with the same object catalogue, but with different seeing values, for a set exposure time of 1 h. For each simulated 8×8 arcmin^2 simulated field, we computed the rms noise $\sigma_{noise} \equiv \sigma_\gamma/\sqrt{N}$, where σ_γ is the rms of shear measures in a single field, and N is the number of usable galaxies in the field. The quantity σ_{noise} is a measure of the uncertainty for measuring the average shear in the field.

The results are shown in Table 2 and Fig. 9. As can be seen in the figure, the seeing degrades the uncertainty almost linearly. Interestingly, the loss of sensitivity comes primarily from the loss in the number N of usable galaxies, with no strong increase observed in σ_{noise} (see Table 2). One might suppose that this degradation could be countered by longer integrations on the field, to regain the number counts diluted by the larger isotropic smear. However, besides the integration time increase being considerable for such a reclamation of number density (see Section 5.5), many of the regained galaxies will still need to be excluded as their shape information has been erased by a kernel significantly larger than their intrinsic radius. The noise could perhaps be reduced by improved shear-measurement methods, which would reduce the cuts we have to make on small galaxies.

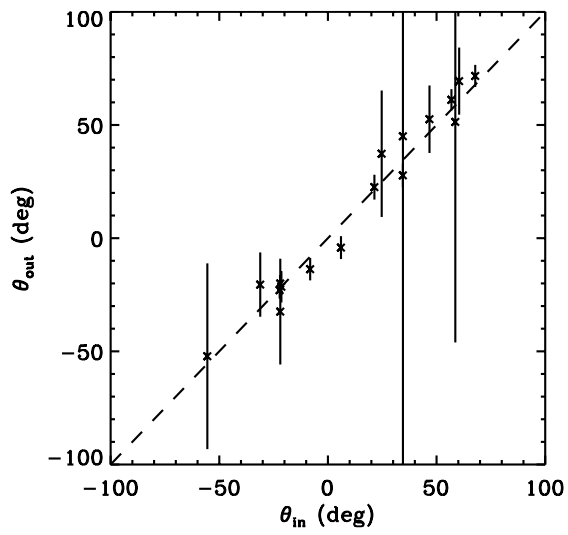

Figure 11. Input shear orientation compared with output shear orientation for simulated data sheared by 5 per cent rms shear in 0.4-arcsec seeing. The dashed line shows the $\theta_{in} = \theta_{out}$ relation, which is the best fit.

Note that, for worse seeing cases, the usable galaxies will be on average brighter and larger and will thus have a lower median redshift. This will tend to degrade the lensing signal further. For a cluster-normalized CDM model, the shear rms from lensing in an 8×8 arcmin^2 cell is $\sigma_{lens} \simeq 0.012 z_m^{0.8}$ (BRE). The median redshift

Table 3. Shear sensitivity as a function of integration time, for 8×8-arcmin^2 cells.

time (s)	n_g (arcmin^{-1})	σ_γ	σ_{noise}	Median R	Median z	σ_{lens}	S/N
1800	11.3	0.43	0.0160	22.9	0.7	0.0086	0.5
2700	16.4	0.42	0.0131	23.4	0.8	0.0096	0.7
3600	18.0	0.44	0.0130	23.4	0.8	0.0096	0.7
4500	20.4	0.42	0.0117	23.6	0.8	0.0096	0.8
5400	22.0	0.42	0.0111	23.8	0.9	0.0106	1.0

is derived from the median *R*-magnitude using the results of Cohen et al. (2000). The resulting lensing rms σ_{lens} is also plotted as a function of seeing in Fig. 9. The reduction of σ_{lens} with seeing is rather weak. The signal-to-noise ratio (S/N) for a single (8×8 arcmin^2) cell, S/N $= \sigma_{lens}/\sigma_{noise}$ is listed in Table 2. The reduction of σ_{lens} with poorer seeing is rather weak. The reduction of S/N for shear measurement is thus again dominated by the decrease in *N*.

In order to check whether the $\gamma_{in} - \gamma_{out}$ relation is comparable for different seeing conditions, we ran a set of 20 simulations with 3 per cent rms shear at a seeing of 0.4 arcsec, to compare with those at 0.8 arcsec above. The results are shown in Fig. 10. Applying a linear regression fit as before, we obtain $\gamma_1^{out} = (0.81 \pm 0.08)\gamma_1^{in}$ and $\gamma_2^{out} = (0.86 \pm 0.05)\gamma_2^{in}$. For the combined components we obtain $\gamma_i^{out} = (0.85 \pm 0.04)\gamma_i^{in}$, consistent with the 0.8-arcsec seeing case. It is encouraging that the correction factors are stable with respect to variations in seeing.

Fig. 11 shows the input versus output orientation of the shear for the 0.4-arcsec simulations. Again, this is unbiased without correction [$\theta_{out} = (1.03 \pm 0.05)\theta_{in}$] and similarly with division by the correction factors [$\theta_{out} = (1.03 \pm 0.05)\theta_{in}$]. This confirms that the KSB calibration is a matter of amplitude correction only, without alteration of orientation.

5.5 Effect of integration time

To optimize weak lensing surveys, one needs to compromise between depth and width. To help in this optimization, we produced several simulated images for different exposure times, while keeping the seeing at 0.8 arcsec. Table 3 shows the quantities discussed in the previous section for different exposure times relevant for ground-based observations. The noise and lensing rms are plotted in Fig. 12. The dependence of these quantities on exposure time is rather weak. This is a result of the fact that the fainter galaxies which can be detected with deeper exposures are too small to be resolved in the presence of seeing, and must therefore be mostly discarded. Moreover, since intrinsic ellipticities dominate the total ellipticity dispersion in this regime (see Section 5.1), the reduced pixel noise of deeper images does not substantially reduce σ_{noise}. As a result, the signal-to-noise ratio to measure lensing is only moderately improved for longer exposures.

5.6 Effect of pixelization

Another test of practical interest is the dependence of the sensitivity to lensing on pixel size. This is important for the design of future dedicated instruments (e.g. Kaiser et al. 2000a; Tyson, Wittman & Angel 2000). To study this dependence in the context of current, ground-based observations, we again produced several simulated fields from the same object catalogue, keeping a seeing FWHM of 0.6 arcsec and exposure time of 1 h, but with different pixel sizes, ranging from 0.1 to 1.0 arcsec.

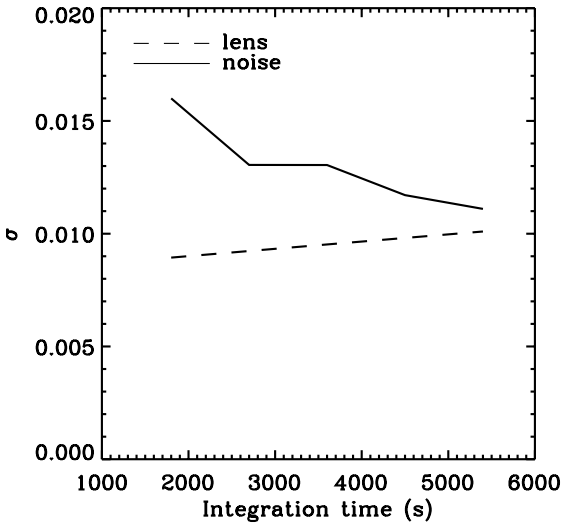

Figure 12. Effect of integration time on the noise (solid) and lensing (dashed) rms.

The results are listed in Table 4 and Fig. 13. We find that the noise is quite stable for pixel scales smaller than the seeing radius. Increased oversampling of the PSF does not improve the noise properties to any great degree. However, as the pixel scale increases above the seeing FWHM, the method fails quickly. The stellar locus on a magnitude–radius plot then approaches the galaxy locus even at bright magnitudes, making star selection for anisotropic smear correction very difficult. Moreover, a pixel scale of, say, 0.8 arcsec with a seeing FWHM of 0.6 arcsec are both conspiring together to remove shape information drastically from galaxies beyond $R \simeq 22$. As a result, σ_{noise} rapidly grows. Extreme oversampling of the PSF appears to be inefficient, while undersampling is very detrimental for typical ground-based seeing. Undersampling is less of a problem for space-based data, however, since the typical pixel scale and PSF FWHM (say 0.1 arcsec) are much smaller than the typical galaxy radius at magnitudes of interest (e.g. Rhodes et al. 2000).

5.7 Small-scale systematic effects

Spurious lensing signals could also be produced on small scales by overlapping isophotes of neighboring galaxies, or by PSF anisotropy residuals. Van Waerbeke et al. (2000) suggested that the overlapping isophote effect could explain the excess small-scale power observed in their cosmic shear survey. To understand this effect, consider two galaxies which, for simplicity, are assumed to be circular. If the galaxies are separated by an angular distance comparable to their angular sizes, their combined isophotes will have a dumb-bell shape rather than be the simple sum of two disjoint circular isophotes. As a result, their ellipticity

Table 4. Shear sensitivity as a function of pixel size, for 8×8-arcmin^2 cells

Pixel ($''$)	n_g (arcmin^{-1})	σ_γ	σ_{noise}	Median R	Median z	σ_{lens}	S/N
0.1	23.9	0.43	0.0126	23.5	0.8	0.0096	0.8
0.2	23.4	0.33	0.0099	23.5	0.8	0.0096	1.0
0.4	21.7	0.35	0.0107	23.4	0.8	0.0096	0.9
0.6	19.5	0.35	0.0114	23.4	0.8	0.0096	0.8
0.8	12.1	1.02	0.0367	23.1	0.7	0.0086	0.2
1.0	13.7	0.66	0.0252	23.0	0.7	0.0086	0.3

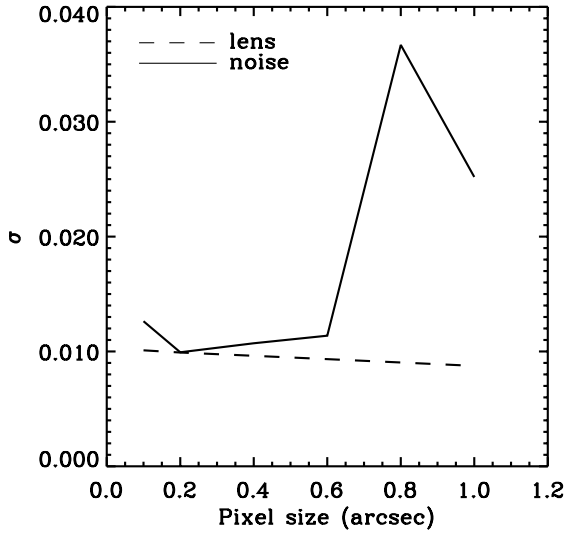

Figure 13. Effect of pixel size on the noise (solid) and lensing (dashed) rms.

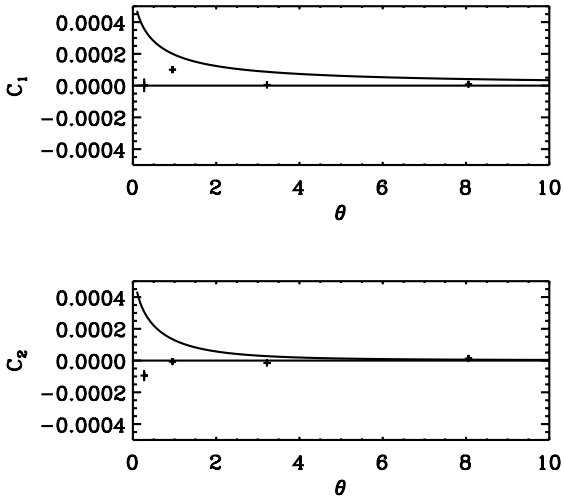

Figure 14. Mean correlation functions C_1 and C_2 for 10 null simulation fields. Points show the mean of 10 correlation functions, with associated uncertainty. The solid curves are the correlation functions for the expected lensing signal for a cluster-normalized ΛCDM cosmology.

will tend to be aligned along the separation axis, leading to a spurious ellipticity correlation.

Furthermore, one might expect a small residual correlation between galaxy shapes at small separations, as a result of the fact that anisotropic PSF correction is implemented with a 2D polynomial fitted upon the stellar PSFs; this will lead to errors in PSF correction typically at scales below the star–star separation ($\simeq$ 1 arcmin).

To test the impact of these effects, we performed 20 simulations without lensing shear (with seeing 0.8 arcsec and exposure time of 1 h). For these simulations, we measured the shear correlation functions defined as (e.g. Kamionkowski et al. 1998)

$$C_{ij}(\theta) \equiv \langle \gamma_i(0) \gamma_j(\theta) \rangle, \tag{7}$$

where i and j run from 1 to 2. Here, $\gamma_i(0)$ and $\gamma_j(\theta)$ are the shear estimates of each member of a galaxy pair with a separation θ. These ellipticities are measured in a coordinate system, the x-axis of which is along the separation angle of the galaxy pair (see Heavens, Refregier & Heymans 2000 for an illustration). After measuring these correlation functions for each of the 20 simulations separately, we computed the mean and error in the mean over all simulations.

The resulting correlation functions are shown in Fig. 14. As a comparison, the correlation function expected from lensing for a cluster-normalized ΛCDM model is also shown (see Heavens et al. 2000 for details of the calculation). In the null simulations we detect a correlation on scales smaller than about 1 arcmin in C_1 and C_2. The amplitude of this effect is $C_i \simeq 10^{-4}$ corresponding to an rms shear of about 1 per cent. As can be seen in Fig. 14, this is considerably smaller than the lensing signal expected on these scales. The exact amplitude of the overlapping isophote effect, plus any other systematic effects present, will depend on the precise conditions of the observation (or simulation). It is nevertheless likely that the excess power observed by van Waerbeke et al. (2000) on small scales ($\theta \lesssim 10$ arcsec) is indeed as a result of these effects.

The C_2 correlation at scales < 0.5 arcmin can be best explained by the overlapping isophote problem described above. The C_1 correlation occurs at slightly larger scales, $0.5 < \theta < 1$ arcmin, and is probably as a result of the errors in PSF correction on the scale of star–star separations.

Apart from residual systematic effects, another explanation for the excess power seen by van Waerbeke et al. (2000) could be the intrinsic alignment of galaxies. Theoretical studies, however, indicate that this effect is small for a survey of this depth (Heavens et al. 2000; Croft & Metzler 2000; see also Catelan, Kamionkowski & Blandford 2001, and Pen, Lee & Seljak 2000).

6 CONCLUSIONS

We have tested our shear measurement method using numerical simulations of artificial images. The object catalogues were created by generating realizations of the *HST* Groth strip; the resulting artificial images include observational effects such as noise, seeing, and anisotropic PSF. We compare our realized catalogues to those observed with WHT and find good statistical agreement. We used these simulations to test the KSB shear measurement method.

Overall, we find that this method is rather accurate, but with several provisos: we find a residual anti-correlation between the PSF ellipticity and the corrected ellipticities of faint galaxies. This effect can be made negligible if faint galaxies (with $S/N \lesssim 15$) are removed from the catalogue. We also find that the recovered shear is linearly related to the input shear, but with a coefficient of about 0.8 which must be used to calibrate the final shear. With these precautions, the KSB method is sufficient for the current weak lensing surveys. However, the method is neither optimal nor necessarily extendable to superior observing conditions. It should therefore be replaced with more accurate methods such as those of Kaiser (2000), Rhodes, Refregier & Groth (2000), and Kuijken (1999) and, in future, more sensitive surveys.

We also used our simulations to study the effect of seeing, exposure time and pixelization on the sensitivity to the shear. We found that increased seeing FWHM increases the noise almost linearly, with the primary loss being the decreased number of usable galaxies. In the seeing-dominated regime, the sensitivity to shear is only weakly dependent on exposure time. As long as this regime holds, it is therefore more efficient to tend towards wide rather than deep weak lensing surveys. Increased pixel scale hardly affects the sensitivity until the pixel scale is comparable to the seeing FWHM, at which point the method fails for typical ground-based seeing. Thus, extreme oversampling of the PSF does not seem to be necessary.

We also tested the claim by van Waerbeke et al. that spurious shear signals on small scales ($\theta \lesssim 10$ arcsec) could be produced by overlapping isophotes of neighboring galaxies. Using simulated images without input shear, we weakly detect small-scale systematics on scales $\theta \lesssim 1$ arcmin. The rms amplitude of the effect is of the order of about 1 per cent, which is smaller than but comparable to that expected for lensing at these scales. Systematic effects at small scales, including those from overlapping isophotes and PSF residuals, are thus likely to explain the excess power found by that group.

ACKNOWLEDGMENTS

We would like to thank Thomas Erben, Peter Schneider, Yannick Mellier, Roberto Maoli and Aurélien Thion for useful discussions. We thank the anonymous referee for his thorough review of our manuscript. We are indebted to Nick Kaiser for providing us with the IMCAT software. We acknowledge the invaluable use of IRAF and SExtractor during this research. AR was supported by a TMR postdoctoral fellowship from the EEC Lensing Network, and by a Wolfson College Research Fellowship. DC acknowledges the 'Sonderforschungsbereich 375-95 für Astro–Teilchenphysik' der Deutschen Forschungsgemeinschaft for financial support. This work was supported by the TMR Network 'Gravitational Lensing: New Constraints on Cosmology and the Distribution of Dark Matter' of the EC under contract No. ERBFMRX-CT97-0172.

REFERENCES

Abraham R. G., Tanvir N. R., Santiago B. X., Ellis R. S., Glazebrook K., van den Bergh S., 1996, MNRAS, 279, L47
Bacon D., Refregier A., Ellis R., 2000, MNRAS, 318, 625 (BRE)
Bartelmann M., Schneider P., 2001, Phys. Rep., 340, 291
Bertin E., Arnoults S., 1996, A&AS, 117, 393
Bonnet H., Mellier Y., 1995, A&A, 303, 331
Catelan P., Kamionkowski M., Blandford R. D., 2001, MNRAS, 320, L7
Cohen J., Hogg D., Blandford R., Cowie L., Hu E., Songaila A., Shopbell P., Richberg K., 2000, ApJ, 538, 29
Croft R. A. C., Metzler C. A., 2000, ApJ, 545, 561
Ebbels T., 1998, PhD thesis. Univ. Cambridge
Erben T., van Waerbeke L., Bertin E., Mellier Y., Schneider P., 2001, A&A, 366, 717
Fort B., Mellier Y., 1994, A&AR, 5, 239
Groth E. J., Kristian J. A., Lynds R., O'Neil E. J., Balsano R., Rhodes J., 1994, BAAS, 185, 5309
Heavens A., Refregier A., Heymans C., 2000, MNRAS, 319, 649
Hoekstra H., Franx M., Kuijken K., Squires G., 1998, ApJ, 504, 636
Hu W., Tegmark M., 1999, ApJ, 514, L65
Jain B., Seljak U., 1997, ApJ, 484, 560
Kaiser N., 1992, ApJ, 388, 272
Kaiser N., 1998, ApJ, 498, 26
Kaiser N., 1999, Review talk for Boston 99 Lensing meeting (preprint astro-ph/9912569)
Kaiser N., 2000, ApJ, 537, 555
Kaiser N., Squires G., Broadhurst T., 1995, ApJ, 449, 460
Kaiser N., Tonry J. L., Luppino G. A., 2000a, PASP, 112, 768
Kaiser N., Wilson G., Luppino A., 2000b (preprint astro-ph/0003338)
Kamionkowski M., Babul A., Cress C., Refregier A., 1998, MNRAS, 301, 1064
Kuijken K., 1999, A&A, 352, 355
Luppino G., Kaiser N., 1997, ApJ, 475, 20
Mellier Y., 1999, ARA&A, 37, 127
Pen U.-L., Lee J., Seljak U., 2000, ApJ, 543, 107
Rhodes J., 1999, PhD thesis, Princeton Univ.
Rhodes J., Refregier A., Groth E., 2000, ApJ, 536, 79
Schneider P., 1996, in Martinez-Gonzalez, Sanz, eds, Universe at High Z. p. 470
Tyson J. A., Wittman D., Angel J. R. P., 2000 (preprint astro-ph/0005381)
van Waerbeke L., Bernardeau F., Mellier Y., 1999, A&A, 342, 15
van Waerbeke L. et al., 2000, A&A, 358, 30
Wittman D., Tyson J. A., Kirkman D., Dell'Antonio I., Bernstein G., 2000, Nat, 405, 143

This paper has been typeset from a TEX/LATEX file prepared by the author.